Computers and Mathematics with Applications 162 (2024) 104–119

Contents lists available at ScienceDirect

Computers and Mathematics with Applications

journal homepage: www.elsevier.com/locate/camwa

An isogeometric shape optimization method for groundwater flow in porous media

Andrea Bressan [a,*], Gabriele Loli [b], Sauro Manenti [c], Alessandro Reali [c,a], Giancarlo Sangalli [b,a]

[a] IMATI-CNR "Enrico Magenes", via Ferrata 5/a, 27100 Pavia, Italy
[b] Department of Mathematics "F. Casorati", University of Pavia, Via Ferrata 1, 27100 Pavia, Italy
[c] Department of Civil Engineering and Architecture (DICAr) and Research Centre on Water (CRA), University of Pavia, Via Ferrata 3, 27100, Pavia, Italy

ARTICLE INFO

Keywords:
Darcy's law
Groundwater flow
Porous media
Isogeometric analysis
Splines
Shape optimization

ABSTRACT

This work introduces a novel isogeometric method for addressing steady, saturated groundwater flow as a free-boundary problem. The innovation lies in adopting a double spline parameterization technique for accurately representing both the porous medium and the fully saturated zone. To linearise the governing equation, we differentiate them with respect to the coefficients of the geometric parameterization. This process results in a quasi-Newton method. Several benchmark numerical tests demonstrate the applicability and effectiveness of the proposed technique.

1. Introduction

Isogeometric Analysis (IGA), firstly introduced in [6,13], is an evolution of classical finite element method (FEM). IGA uses splines, Non-Uniform Rational B-splines (NURBS), and other possible generalizations, both for the parameterization of the computational domain, as typically done in computer aided design (CAD), see [20], and for the representation of the unknown field of the differential problem of interest. One of the advantages of IGA is that, thanks to a possibly exact (or in any case highly accurate) representation of the computational domain, errors due to the approximation of the geometry can be eliminated (or significantly limited). IGA also benefits from the approximation properties of splines, whose high-continuity yields higher accuracy when compared to standard FEM, see [5,10].

In what follows, we are interested in devising a numerical method for the solution of a steady, saturated groundwater flow problem. Groundwater flow refers to the filtration of water beneath ground surface. This movement is influenced by various factors such as topography, geology, porosity and on the hydraulic conductivity $\boldsymbol{K}$, which is related to the properties of solid matrix (i.e., the permeability κ) and of fluid phase (i.e., the kinematic viscosity ν), see [3]. The study of groundwater flow is crucial in hydrogeology because it is involved in many important processes, such as erosion, stability of slopes, waterlogging, and the movement of contaminants through the ground. For these reasons, an accurate determination of groundwater flow is essential for designing structures and managing water resources. For a deeper description of the topic we refer to [2,12].

IGA has been already successfully applied to the study of groundwater flow. In particular, in [19,26,27] the authors present isogeometric methods for transient groundwater flow in unsaturated porous media, which means that voids may be filled by a mixture of two or more fluid phases. In this case, the balance equation for the mixture should be solved to obtain the flow field. Richards' equation represents a simplified version of the balance equation that provides approximate description of the water seepage in the unsaturated zone, assuming negligible pressure gradients in the gas phase and nearly isothermal conditions, see [21]. In the analysis of some classes of free surface flow problems the interface may undergo large and rapid deformations causing fluid splitting/merging which require proper numerical schemes to be handled, see [22–24]. On the other hand, in the case of saturated porous media, topological changes such as fissuring and merger of the free surface do not play a role as the phreatic surface can be considered an impervious, sharp regular interface, the uppermost geometrical flow boundary, dividing a fully saturated from a fully dry zone. Once this assumption is made, the form of the equations can vary with respect to whether compressibility effects are considered or not, and with respect to the flow law used. For instance, when both solid matrix and water are assumed to be incompressible and the flow obeys Darcy's

* Corresponding author.
E-mail addresses: andrea.bressan@imati.cnr.it (A. Bressan), gabriele.loli@unipv.it (G. Loli), sauro.manenti@unipv.it (S. Manenti), alereali@unipv.it (A. Reali), giancarlo.sangalli@unipv.it (G. Sangalli).

https://doi.org/10.1016/j.camwa.2024.02.044
Received 30 November 2023; Accepted 25 February 2024
Available online 15 March 2024

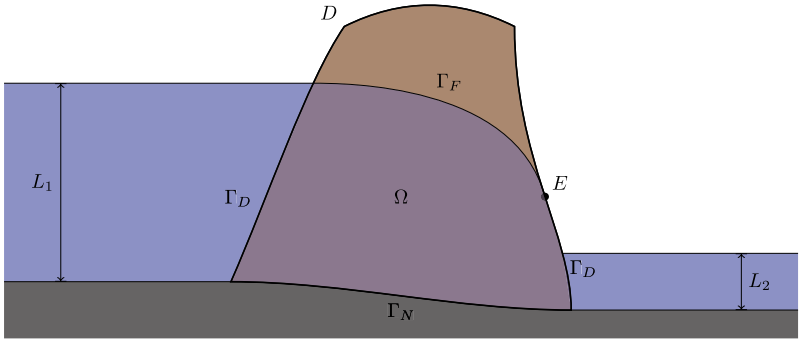

Fig. 1. Earth dam example.

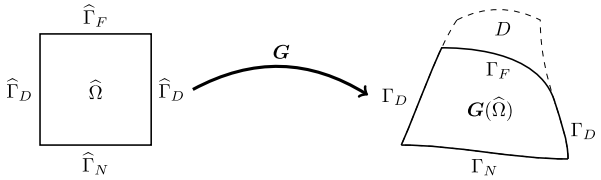

Fig. 2. Example of parameterization for the wet region.

law, the steady-state flow of water for a homogeneous, isotropic and saturated soil is described by the well-known Laplace and Poisson equations in the absence or presence of sources and sinks, respectively. Along the phreatic surface that, according to this approach, constitutes a geometrical boundary of the flow domain, two boundary conditions have to be satisfied: the pressure head must be atmospheric and the velocity of the free surface must be equal to the discharge (or recharge) velocity of the fluid normal to the surface, divided by the effective porosity. The shape of the phreatic surface is itself an unknown of the problem, to be found during the solution. This class of problems, containing an unknown geometrical limit, constitute a distinct category of mathematical problems, known as free boundary problems. Numerical methods for free boundary problems, based on classical Finite Difference, Finite Volume, or Finite Element Methods, can be found in [1,4,9,11,14,17,29]. Isogeometric analysis of free boundary problems arising in groundwater flow has been considered in more recent works, such as [15,18,30,31].

In this work, we propose a new isogeometric method for the steady, saturated groundwater flow formulated as a free-boundary problem. The novelty of our approach is to exploit a double spline parameterization of the computational domain in order to exactly describe both the porous medium and the fully saturated zone. In particular, we first consider a spline parameterization of the whole porous medium. Then, we compose it with a spline map that describes the saturated portion of the physical domain. This second parameterization represents one of the unknowns of the problem, together with the water flux. Following shape calculus techniques, as described for example in [8,28], in order to linearize the governing equations with respect to the geometry, we differentiate them with respect to the coefficients of the parameterization, also known as *control points*, of the wet domain. In this way, we obtain a quasi-Newton method. Eventually, a set of numerical tests in 2D and 3D clearly shows the effectiveness of the proposed formulation.

The structure of the paper is as follows. Section 2 briefly introduces the differential free boundary problem, governing groundwater flow in saturated porous media, and its variational formulation. In Section 3 we recall fundamental concepts and notations related to B-splines and Isogeometric Analysis. Section 4 describes in details the isogeometric formulation of the problem and the derivation of the proposed method for solving it. In Section 5 the method is validated on several numerical benchmarks. Finally, some conclusions are outlined in Section 6.

2. Model problem

As a model problem, we consider the unconfined water flow with seepage through a porous medium, as depicted in Fig. 1. Given a domain $D \subset \mathbb{R}^d$, $d = 2, 3$, representing a porous portion of the ground, we assume that the wet part $\Omega \subset D$ is parametrized by a function $\boldsymbol{G} : [0,1]^d \to D$, namely $\Omega = \boldsymbol{G}(\widehat{\Omega})$, where we have defined $\widehat{\Omega} := [0,1]^d$, see Fig. 2 for an example. The coordinates on $\widehat{\Omega}$ are $\boldsymbol{\zeta} = (\zeta_1, \dots, \zeta_d)$ and those on D are $\boldsymbol{x} = (x_1, \dots, x_d)$. The function $h : \Omega \to \mathbb{R}$ is the piezometric head, representing the fluid energy density, and satisfies the following system of equations, derived from the Darcy law and mass conservation,

$$\begin{cases} -\operatorname{div} \boldsymbol{K} \nabla h = f & \text{on } \Omega \\ h(\boldsymbol{x}) = x_d & \text{on } \Gamma_F \\ \boldsymbol{K} \nabla h \cdot \boldsymbol{n} = \boldsymbol{r} \cdot \boldsymbol{n} & \text{on } \Gamma_F \\ h = \ell & \text{on } \Gamma_D \\ \boldsymbol{K} \nabla h \cdot \boldsymbol{n} = 0 & \text{on } \Gamma_N \end{cases} \tag{2.1}$$

where

- $\boldsymbol{K} \in L^\infty(D, \mathbb{R}^{d \times d})$ describes the *hydraulic conductivity* of the ground;
- $f \in L^\infty(D)$ represents the water source;
- $\boldsymbol{n}$ is the unit normal vector to $\boldsymbol{G}(\zeta_1, \dots, \zeta_{d-1}, 1)$;
- $\boldsymbol{r} \in L^\infty(\mathbb{R}^d, \mathbb{R}^d)$, also known as *recharge*, is the density of water flux accounting for the percolation of rain and evaporation;

- ℓ is a prescribed water level in the reservoirs;
- Γ_D is the part of the boundary in contact with reservoirs or rivers;
- Γ_N is the impervious layer below the aquifer;
- $\Gamma_F := \{\boldsymbol{x} = \boldsymbol{G}(\zeta_1, \dots, \zeta_{d-1}, 1) \in \mathbb{R}^d\}$ is the free boundary.

Remark 1. In order to allow for seepage, if $L : \Gamma_D \to \mathbb{R}$ represents the piezometric head of the reservoirs in contact with Γ_D, then the prescribed water level ℓ should be

$$\ell(\boldsymbol{x}) := \max\{L(\boldsymbol{x}), x_d\}.$$

2.1. Variational formulation

A possible weak formulation for (2.1) reads as follows.
Find $(\boldsymbol{G}, h) \in \left([H^1(\widehat{\Omega})]^d, H^1(\Omega)\right)$ such that:

$$\begin{cases} \displaystyle\int_\Omega \nabla v \boldsymbol{K} \nabla h^T = \int_\Omega f v + \int_{\Gamma_F} (\boldsymbol{r}\cdot\boldsymbol{n}) v, & \forall v \in H^1_{0,\Gamma_D}(\Omega) \\ \displaystyle\int_{\Gamma_D} (h-\ell) w = 0, & \forall w \in L^2(\Gamma_D) \\ \displaystyle\int_{\Gamma_F} (h - x_d)\varphi = 0, & \forall \varphi \in L^2(\Gamma_F) \end{cases} \tag{2.2}$$

Defining $\widehat{h} = h\circ\boldsymbol{G}$, $\widehat{w} = w\circ\boldsymbol{G}$, $\widehat{\boldsymbol{K}} = \boldsymbol{K}\circ\boldsymbol{G}$, $\widehat{\boldsymbol{r}} = \boldsymbol{r}\circ\boldsymbol{G}$ and $\widehat{\ell} = \ell\circ\boldsymbol{G}$, we can pullback the equations on $\widehat{\Omega}$ and obtain the following problem.
Find $(\boldsymbol{G}, \widehat{h}) \in \left([H^1(\widehat{\Omega})]^d, H^1(\widehat{\Omega})\right)$ such that:

$$\begin{cases} \displaystyle\int_{\widehat{\Omega}} (\nabla\widehat{v}) \boldsymbol{J}_G^{-1} \widehat{\boldsymbol{K}} \boldsymbol{J}_G^{-T} \nabla\widehat{h}^T \det \boldsymbol{J}_G = \int_{\widehat{\Omega}} \widehat{f}\widehat{v} \det \boldsymbol{J}_G + \int_{\widehat{\Gamma_F}} (\widehat{\boldsymbol{r}}\cdot\widehat{\boldsymbol{n}})\widehat{v} \det \boldsymbol{J}_{\widehat{\Gamma}_F}, & \forall \widehat{v} \in H^1_{0,\widehat{\Gamma}_D}(\widehat{\Omega}) \\ \displaystyle\int_{\widehat{\Gamma}_D} (\widehat{h} - \widehat{\ell})\widehat{w} \det \boldsymbol{J}_{\widehat{\Gamma}_D} = 0, & \forall \widehat{w} \in L^2(\widehat{\Gamma}_D) \\ \displaystyle\int_{\widehat{\Gamma}_F} (\widehat{h} - \widehat{x}_d)\widehat{\varphi} \det \boldsymbol{J}_{\widehat{\Gamma}_F} = 0, & \forall \widehat{\varphi} \in L^2(\widehat{\Gamma}_F) \end{cases} \tag{2.3}$$

where

- $\widehat{\Gamma}_D := \boldsymbol{G}^{-1}(\Gamma_D)$ are the lateral boundary of the parametric domain;
- $\widehat{\Gamma}_F := \boldsymbol{G}^{-1}(\Gamma_F)$ is the top boundary of the parametric domain;
- $\boldsymbol{J}_G$ is the Jacobian matrix of $\boldsymbol{G}$;
- $\boldsymbol{J}_{\widehat{\Gamma}_D}$ is the surface Jacobian matrix of $\boldsymbol{G}$ on $\widehat{\Gamma}_D$;
- $\boldsymbol{J}_{\widehat{\Gamma}_F}$ is the surface Jacobian matrix of $\boldsymbol{G}$ on $\widehat{\Gamma}_F$.

3. Preliminaries on isogeometric analysis

3.1. B-splines

Given two positive integers p and m, consider an open knot vector $\Xi := \{\xi_1, \dots, \xi_{m+p+1}\}$ such that

$$\xi_1 = \dots = \xi_{p+1} < \xi_{p+2} \le \dots \le \xi_m < \xi_{m+1} = \dots = \xi_{m+p+1},$$

where interior repeated knots are allowed with maximum multiplicity p. Without loss of generality, we assume $\xi_1 = 0$ and $\xi_{m+p+1} = 1$. From the knot vector Ξ, B-spline functions of degree p are defined following the well-known Cox-De Boor recursive formula: we start with piecewise constants ($p = 0$):

$$\widehat{b}_{i,0}(\zeta) = \begin{cases} 1 & \text{if } \xi_i \le \zeta < \xi_{i+1}, \\ 0 & \text{otherwise,} \end{cases}$$

and for $p \ge 1$ the B-spline functions are defined by the recursion

$$\widehat{b}_{i,p}(\zeta) = \frac{\zeta - \xi_i}{\xi_{i+p} - \xi_i}\widehat{b}_{i,p-1}(\zeta) + \frac{\xi_{i+p+1} - \zeta}{\xi_{i+p+1} - \xi_{i+1}}\widehat{b}_{i+1,p-1}(\zeta),$$

where $0/0 = 0$. The univariate spline space is defined as

$$\widehat{\mathcal{S}}_\tau = \widehat{\mathcal{S}}_\tau([0,1]) := \operatorname{span}\{\widehat{b}_{i,p}\}_{i=1}^m,$$

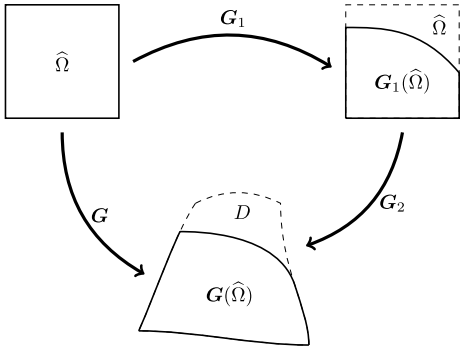

Fig. 3. Scheme of the double parametrization.

where τ denotes the maximal mesh-size, that is

$$\tau := \max_{1\le i\le m+p+1} \{|\xi_{k,i+1} - \xi_{k,i}|\}.$$

For brevity, the degree p is not always reported in the notation. For more details of B-splines properties see [6,7].

Multivariate B-splines are defined from univariate B-splines by tensorization. Let d be the space dimension, we consider d open knot vectors $\Xi_k = \{\xi_{k,1}, \dots, \xi_{k,m_k+p_k+1}\}$, for $k = 1, \dots, d$, and a set of multi-indices $\mathbf{I} := \{\mathbf{i} = (i_1, \dots, i_d) : 1 \le i_k \le m_k\}$. For each multi-index $\mathbf{i} = (i_1, \dots, i_d)$, we introduce the d-variate B-spline,

$$\widehat{B}_{\mathbf{i}}(\zeta) := \widehat{b}[\Xi_{i_1,p_1}](\zeta_1) \dots \widehat{b}[\Xi_{i_d,p_d}](\zeta_d).$$

The corresponding spline space is defined as

$$\widehat{S}_\tau = \widehat{S}_\tau([0,1]^d) := \operatorname{span}\left\{ B_{\mathbf{i}} : \mathbf{i} \in \mathbf{I} \right\},$$

where τ is the maximal mesh-size in all knot vectors.

3.2. Isogeometric spaces

Let us consider a single patch domain $\Omega \subset \mathbb{R}^d$, given by a d-dimensional spline parameterization $\boldsymbol{G}$, that is

$$\Omega = \boldsymbol{G}(\widehat{\Omega}), \qquad \text{with } \boldsymbol{G}(\boldsymbol{\zeta}) = \sum_{\mathbf{i}} \boldsymbol{C}_{\mathbf{i}} \widehat{B}_{\mathbf{i}}(\boldsymbol{\zeta}),$$

where $\boldsymbol{C}_{\mathbf{i}}$ are the control points and $\widehat{B}_{\mathbf{i}}$ are tensor-product B-spline basis functions defined on the parametric patch $\widehat{\Omega} := (0,1)^d$. Following the isoparametric paradigm, the isogeometric basis functions $B_{\mathbf{i}}$ are defined as $B_{\mathbf{i}} = \widehat{B}_{\mathbf{i}} \circ \boldsymbol{G}^{-1}$. Thus, the isogeometric space on Ω is defined as

$$S_\tau = S_\tau(\Omega) := \operatorname{span}\left\{ B_{\mathbf{i}} := \widehat{B}_{\mathbf{i}} \circ \boldsymbol{G}^{-1} \ : \ \mathbf{i} \in \mathbf{I} \right\}.$$

By introducing a co-lexicographical reordering of the basis functions, with a minor abuse of notation we will also write in what follows

$$S_\tau = \operatorname{span}\left\{ B_{\mathbf{i}} : \mathbf{i} \in \mathbf{I} \right\} = \operatorname{span}\left\{ B_i \right\}_{i=1}^{N_{\text{dof}}}.$$

4. Discrete formulation

Assume that the terrain D is described by a parametrization $\boldsymbol{G}_2 : [0,1]^d \to \mathbb{R}^d$ that is either provided by CAD or obtained by approximating measured terrain data. To obtain an isogeometric discretization of (2.2), we look for a parametrization $\boldsymbol{G}$ of the wet domain having the form $\boldsymbol{G} = \boldsymbol{G}_2 \circ \boldsymbol{G}_1$. Here, $\boldsymbol{G}_2 : \widehat{\Omega} \to D$ is the fixed parametrization of the physical domain D, while $\boldsymbol{G}_1 : \widehat{\Omega} \to \widehat{\Omega}$ is an unknown map that parametrizes a subset of $\widehat{\Omega}$. In this way, $\boldsymbol{G}_1(\widehat{\Omega})$ turns out to be the preimage under $\boldsymbol{G}_2$ of the wet portion of D, as shown in Fig. 3.

Further we take $\boldsymbol{G}_1$ to preserve the first $d-1$ components (Fig. 4) so that the preimage under $\boldsymbol{G}_2$ of the phreatic surface Γ_F is the graph of a function, that is: there exists a continuous function $\varphi : [0,1]^{d-1} \to (0,1]$ such that

$$\boldsymbol{G}_2^{-1}(\Gamma_F) = \boldsymbol{G}_1([0,1]^{d-1} \times \{1\}) = \left\{ (\boldsymbol{\zeta}, \varphi(\boldsymbol{\zeta})) : \boldsymbol{\zeta} \in [0,1]^{d-1} \right\}.$$

More precisely, we consider $\boldsymbol{G}_1 \in \mathcal{V}_{\tau_g}$, where $\mathcal{V}_{\tau_g}$ is defined as follows:

$$\mathcal{V}_{\tau_g} := \left\{ (\zeta_1, \dots, \zeta_d) \longmapsto \left(\zeta_1, \dots, \zeta_{d-1}, \zeta_d \sum_{i=1}^{N_g} \alpha_i \widehat{B}_i^g(\zeta_1, \dots, \zeta_{d-1}) \right) : \boldsymbol{\alpha} \in \mathbb{R}^{N_g}, \widehat{B}_i^g \in \mathcal{S}_{\tau_g}^p([0,1]^{d-1}) \right\},$$

for some spline space $\mathcal{S}_{\tau_g}^p([0,1]^{d-1})$. By considering another spline space for the piezometric head h, namely

$$\mathcal{X}_{\tau_h} := \mathcal{S}_{\tau_h}^p([0,1]^d) = \operatorname{span}\left\{ \widehat{B}_i^h \mid i = 1, \dots, N_h \right\},$$

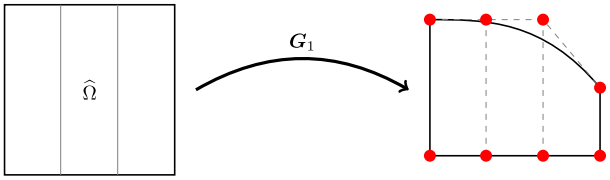

Fig. 4. Example of parametrization of the wet region with $p = 3$. Red circles represent the control points of $\boldsymbol{G}_1$.

a discrete version of the weak formulation (2.3) can be expressed as follows.

Find $(\boldsymbol{G}_1, \widehat{h}_\tau) \in \left(\mathcal{V}_{\tau_g}, \mathcal{X}_{\tau_h}\right)$ such that:

$$\begin{cases} \displaystyle\int_{\widehat{\Omega}} (\nabla \widehat{v}) \boldsymbol{J}_G^{-1} \widehat{\boldsymbol{K}} \boldsymbol{J}_G^{-T} \nabla \widehat{h}_\tau^T \det \boldsymbol{J}_G = \int_{\widehat{\Omega}} \widehat{f} \widehat{v} \det \boldsymbol{J}_G + \int_{\widehat{\Gamma_F}} (\widehat{\boldsymbol{r}} \cdot \widehat{\boldsymbol{n}}) \widehat{v} \det \boldsymbol{J}_{\widehat{\Gamma}_F}, & \forall \widehat{v} \in \mathcal{X}_{\tau_h} \cap H^1_{0,\widehat{\Gamma}_D}(\widehat{\Omega}) \\ \displaystyle\int_{\widehat{\Gamma}_D} (\widehat{h}_\tau - \widehat{\ell}) \widehat{w} \det \boldsymbol{J}_{\widehat{\Gamma}_D} = 0, & \forall \widehat{w} \in S^p_{\tau_h}(\widehat{\Gamma}_D) \\ \displaystyle\int_{\widehat{\Gamma}_F} (\widehat{h}_\tau - \widehat{x}_d) \widehat{\varphi} \det \boldsymbol{J}_{\widehat{\Gamma}_F} = 0, & \forall \widehat{\varphi} \in S^p_{\tau_g}(\widehat{\Gamma}_F). \end{cases} \tag{4.1}$$

It's important to note that the third equation in (4.1) also depends on the derivative of the pullback of the Lebesgue measure on the physical domain $\det \boldsymbol{J}_{\widehat{\Gamma}_F}$. Minimizing the error on this equation can lead to paradoxical results where the error is minimized by reducing volumes or surface areas. For this reason, since $\det \boldsymbol{J}_{\widehat{\Gamma}_F} > 0$, we can neglect it and obtain the following alternative formulation.

Find $(\boldsymbol{G}_1, \widehat{h}_\tau) \in \left(\mathcal{V}_{\tau_g}, \mathcal{X}_{\tau_h}\right)$ such that:

$$\begin{cases} \displaystyle\int_{\widehat{\Omega}} (\nabla \widehat{v}) \boldsymbol{J}_G^{-1} \widehat{\boldsymbol{K}} \boldsymbol{J}_G^{-T} \nabla \widehat{h}_\tau^T \det \boldsymbol{J}_G = \int_{\widehat{\Omega}} \widehat{f} \widehat{v} \det \boldsymbol{J}_G + \int_{\widehat{\Gamma_F}} (\widehat{\boldsymbol{r}} \cdot \widehat{\boldsymbol{n}}) \widehat{v} \det \boldsymbol{J}_{\widehat{\Gamma}_F}, & \forall \widehat{v} \in \mathcal{X}_{\tau_h} \cap H^1_{0,\widehat{\Gamma}_D}(\widehat{\Omega}) \\ \displaystyle\int_{\widehat{\Gamma}_D} (\widehat{h}_\tau - \widehat{\ell}) \widehat{w} \det \boldsymbol{J}_{\widehat{\Gamma}_D} = 0, & \forall \widehat{w} \in S^p_{\tau_h}(\widehat{\Gamma}_D) \\ \displaystyle\int_{\widehat{\Gamma}_F} (\widehat{h}_\tau - \widehat{x}_d) \widehat{\varphi} = 0, & \forall \widehat{\varphi} \in S^p_{\tau_g}(\widehat{\Gamma}_F). \end{cases} \tag{4.2}$$

Remark 2. This choice of the discretization restricts our analysis to those wet regions $\boldsymbol{G}(\widehat{\Omega})$ that are homeomorphic to $\widehat{\Omega}$. This implies that, for example, no internal dry regions are allowed.

4.1. Quasi-Newton method

In order to illustrate a numerical method for solving (4.2), let us define

$$\boldsymbol{F} = (\boldsymbol{F}_1, \boldsymbol{F}_2, \boldsymbol{F}_3) : \left(\mathcal{V}_{\tau_g} \times \mathcal{X}_{\tau_h}\right) \to \mathbb{R}^{N_g + N_h},$$

with

$$\boldsymbol{F}_{1,i}(\boldsymbol{\alpha}, \widehat{h}_\tau) := \int_{\widehat{\Omega}} (\nabla \widehat{B}_i^h) \boldsymbol{J}_G^{-1} \widehat{\boldsymbol{K}} \boldsymbol{J}_G^{-T} \nabla \widehat{h}_\tau^T \det \boldsymbol{J}_G - \int_{\widehat{\Omega}} \widehat{f} \widehat{B}_i^h \det \boldsymbol{J}_G + \int_{\widehat{\Gamma_F}} (\widehat{\boldsymbol{r}} \cdot \widehat{\boldsymbol{n}}) \widehat{B}_i^h \det \boldsymbol{J}_{\widehat{\Gamma}_F},$$

$$\boldsymbol{F}_{2,j}(\boldsymbol{\alpha}, \widehat{h}_\tau) := \int_{\widehat{\Gamma}_D} (\widehat{h}_\tau - \widehat{\ell}) \widehat{B}_j^h \det \boldsymbol{J}_{\widehat{\Gamma}_D},$$

$$\boldsymbol{F}_{3,k}(\boldsymbol{\alpha}, \widehat{h}_\tau) := \int_{\widehat{\Gamma}_F} (\widehat{h}_\tau - \widehat{x}_d) \widehat{B}_k^g,$$

where the dependence on $\boldsymbol{\alpha}$ arises from the presence of the Jacobian matrix $\boldsymbol{J}_G$ and the composition of $\boldsymbol{K}$, f, $\boldsymbol{r}$, $\boldsymbol{n}$, ℓ, x_d with $\boldsymbol{G}$.

Solving (4.2) is equivalent to solve

$$\boldsymbol{F}(\boldsymbol{\alpha}, \widehat{h}_\tau) = \boldsymbol{0}. \tag{4.3}$$

Since the dependence of $\boldsymbol{F}$ on α_i is non-linear, we propose a quasi-Newton method for solving (4.3). A step of Newton method for $\boldsymbol{F} = \boldsymbol{0}$ starting from $(\boldsymbol{\alpha}^{(0)}, \widehat{h}_\tau^{(0)})$ is

$$(\boldsymbol{\alpha}^{(i+1)}, \hat{h}_\tau^{(i+1)}) = (\boldsymbol{\alpha}^{(i)}, \hat{h}_\tau^{(i)}) - \nabla \boldsymbol{F}(\boldsymbol{\alpha}^{(i)}, \hat{h}_\tau^{(i)})^{-1} \boldsymbol{F}(\boldsymbol{\alpha}^{(i)}, \hat{h}_\tau^{(i)}). \tag{4.4}$$

The computation of $\nabla \boldsymbol{F}$ is computationally expensive and it can be avoided by using a quasi-Newton scheme. Indeed, for a fixed $\boldsymbol{\alpha}$, equation (4.3) is linear with respect to $\hat{h}_\tau$ and it reads: find $\hat{h}_\tau \in \mathcal{X}_\tau$ such that:

$$\begin{cases} \displaystyle\int_{\hat{\Omega}} (\nabla \hat{v}) \boldsymbol{J}_G^{-1} \hat{\boldsymbol{K}} \boldsymbol{J}_G^{-T} \nabla \hat{h}_\tau^T \det \boldsymbol{J}_G = \int_{\hat{\Omega}} \hat{f} \hat{v} \det \boldsymbol{J}_G + \int_{\widehat{\Gamma_F}} (\hat{\boldsymbol{r}} \cdot \hat{\boldsymbol{n}}) \hat{v} \det \boldsymbol{J}_{\hat{\Gamma}_F}, & \forall \hat{v} \in \mathcal{X}_{\tau_h} \cap H^1_{0,\hat{\Gamma}_D}(\hat{\Omega}) \\ \displaystyle\int_{\hat{\Gamma}_D} (\hat{h}_\tau - \hat{\ell}) \hat{w} \det \boldsymbol{J}_{\hat{\Gamma}_D} = 0, & \forall \hat{w} \in S^p_{\tau_h}(\hat{\Gamma}_D). \end{cases} \tag{4.5}$$

This suggests to restrict the problem on the parametric space $\mathcal{V}_{\tau_g} \times \mathcal{X}_{\tau_h}$ to the manifold

$$\mathcal{M} := \{(\hat{h}_\tau, \boldsymbol{\alpha}) \in \mathcal{V}_{\tau_g} \times \mathcal{X}_{\tau_h} : \hat{h}_\tau \text{ solves (4.5)}\}.$$

Starting from a point in $(\boldsymbol{\alpha}^{(i)}, \hat{h}_\tau^{(i)}) \in \mathcal{M}$ the quasi-Newton step is defined as solving

$$\boldsymbol{\alpha}^{(i+1)} = \boldsymbol{\alpha}^{(i)} - \nabla_{\boldsymbol{\alpha}} \boldsymbol{F}_3(\boldsymbol{\alpha}^{(i)}, \hat{h}_\tau^{(i)})^{-1} \boldsymbol{F}_3(\boldsymbol{\alpha}^{(i)}, \hat{h}_\tau^{(i)})$$

and then obtaining a point in $\mathcal{M}$ by solving (4.5) with $\boldsymbol{G}^{(i+1)}$ to obtain $\hat{h}_\tau^{(i+1)}$. The stopping criterion we propose is based on the L^∞-norm of the Newton method step for $\boldsymbol{F}_3$. The proposed quasi-Newton method for solving (4.3) can be summarized as in Algorithm 1.

Algorithm 1 Quasi-Newton method.

Choose an initial guess $\boldsymbol{\alpha}^{(0)}$ and a tolerance ϵ
repeat
  Given $\boldsymbol{\alpha}^{(n)}$, find $\hat{h}_\tau^{(n)}$ such that $\left(\boldsymbol{F}_1(\boldsymbol{\alpha}^{(n)}, \hat{h}_\tau^{(n)}), \boldsymbol{F}_2(\boldsymbol{\alpha}^{(n)}, \hat{h}_\tau^{(n)})\right) = \boldsymbol{0}$
  Compute $\boldsymbol{\alpha}^{(n+1)}$ as

$$\boldsymbol{\alpha}^{(n+1)} = \boldsymbol{\alpha}^{(n)} - \nabla_{\boldsymbol{\alpha}} \boldsymbol{F}_3(\boldsymbol{\alpha}^{(n)}, \hat{h}_\tau^{(n)})^{-1} \boldsymbol{F}_3(\boldsymbol{\alpha}^{(n)}, \hat{h}_\tau^{(n)})$$

until $\|\nabla_{\boldsymbol{\alpha}} \boldsymbol{F}_3(\boldsymbol{\alpha}^{(n+1)}, \hat{h}_\tau^{(n+1)})^{-1} \boldsymbol{F}_3(\boldsymbol{\alpha}^{(n+1)}, \hat{h}_\tau^{(n+1)})\|_\infty \le \epsilon$

Denoting $\hat{x}_d(\boldsymbol{\zeta}) = (x_d \circ G)(\boldsymbol{\zeta})$, it follows that

$$\begin{aligned} \partial_{\boldsymbol{\alpha}_m} \hat{x}_d &= \nabla x_d \nabla \boldsymbol{G}_2 \partial_{\boldsymbol{\alpha}_m} \boldsymbol{G}_1(\boldsymbol{\zeta}) \\ &= \boldsymbol{e}_d^T \nabla \boldsymbol{G}_2 \cdot \left(\boldsymbol{0}, \zeta_d \hat{B}^g_m(\zeta_1, \dots, \zeta_{d-1})\right)^T \\ &= \boldsymbol{e}_d^T \nabla \boldsymbol{G}_2 \boldsymbol{e}_d \zeta_d \hat{B}^g_m(\zeta_1, \dots, \zeta_{d-1}). \end{aligned}$$

Keeping that in mind, we observe that $\nabla_{\boldsymbol{\alpha}} \boldsymbol{F}_3$ is a weighted mass matrix defined on $S^p_{\tau_g}([0,1]^{d-1})$. In fact, it holds:

$$\partial_{\boldsymbol{\alpha}_m} \boldsymbol{F}_{3,k}(\boldsymbol{\alpha}, \hat{y}) = \partial_{\boldsymbol{\alpha}_m} \int_{\hat{\Gamma}_F} (\hat{y} - \hat{x}_d) \hat{B}^g_k = \int_{\hat{\Gamma}_F} -\partial_{\boldsymbol{\alpha}_m}(\hat{x}_d) \hat{B}^g_k = \int_{\hat{\Gamma}_F} -\boldsymbol{e}_d^T \nabla \boldsymbol{G}_2 \boldsymbol{e}_d \hat{B}^g_m \hat{B}^g_k.$$

The iteration described above does not work in general. To understand why it is instructive to consider the simplified case when $\boldsymbol{G}_2$ is the identity and the last component of $\boldsymbol{G}_1(\cdot, 1)$ is in the same spline space as $\hat{h}_\tau|_{\hat{\Gamma}_F}$. In this case the update of $\boldsymbol{G}_1$ equals $(\hat{h}_\tau - \hat{x}_d)|_{\hat{\Gamma}_F}$ and, since the restriction $(\hat{h}_\tau - \hat{x}_d)|_{\partial\hat{\Gamma}_F}$ vanishes because of the Dirichlet conditions, the value of $\boldsymbol{G}_1$ on $\partial\hat{\Gamma}_F$ is fixed at the first iteration. That is: it is impossible to deduce information about the real solution where wrong information has been forced at the current step.

The problem can be solved in different ways. An approach is to change the geometry update for the degrees of freedom that do not vanish on $\partial\hat{\Gamma}_F$. This is done in [15] where the 'locking" effect is avoided by updating $\boldsymbol{G}_1$ on $\partial\hat{\Gamma}_F$ based on the normal flow condition on the free boundary.

Here we choose a different solution: the space $S^p_{\tau_h}$ in the neighborhood of $\partial\hat{\Gamma}_F$ is enriched by τ-refinement so that the weighted L^2-projection is not exact close to $\partial\hat{\Gamma}_F$. This approach is justified by the fact that the solution $\hat{h}|_{\hat{\Gamma}_F}$ on an inexact geometry behaves as fractional power of the distance from $\partial\hat{\Gamma}_F$. By increasing the resolution for h the projection will then average h and move $\partial\Gamma_F$ in the right direction.

In order to speed up the convergence of Algorithm 1, we propose a progressive refinement of the spline spaces $S^p_{\tau_g}$ and $S^p_{\tau_h}$, until we reach a desired value for the mesh size $\tau_{\min}$. The accelerated version of the algorithm is summarized in Algorithm 2.

Remark 3. The computational efficiency of both Algorithms 1 and 2 can be significantly enhanced through the utilization of appropriate, efficient solvers, based on preconditioned version of Conjugate Gradient Method or other Krylov subspace methods. Specifically, the determination of $\hat{h}_\tau^{(n)}$, which involves the solution of the Laplace boundary value problem (4.5), can be substantially expedited by leveraging the preconditioners outlined in [25]. For what concerns the computation of the geometry update $\boldsymbol{\alpha}^{(n+1)}$, the linear system associated to the weighted isogeometric mass matrix $\nabla_{\boldsymbol{\alpha}} \boldsymbol{F}_3(\boldsymbol{\alpha}^{(n)}, \hat{h}_\tau^{(n)})$ can be preconditioned following the methodology delineated in [16]. Finally, for reducing the computational cost required for assembling the matrix $\nabla_{\boldsymbol{\alpha}} \boldsymbol{F}_3(\boldsymbol{\alpha}^{(n)}, \hat{h}_\tau^{(n)})$, one can rely on Broyden or Anderson accelerations.

Algorithm 2 Accelerated Quasi-Newton method.

Choose initial spline spaces $\mathcal{S}^p_{\tau_g}$, $\mathcal{S}^p_{\tau_h}$, an initial guess $\boldsymbol{\alpha}^{(0)}$ and a target mesh-size $\tau_{\min}$
repeat
  repeat
    Given $\boldsymbol{\alpha}^{(n)}$, find $\widehat{h}^{(n)}_\tau$ such that $\left(\boldsymbol{F}_1(\boldsymbol{\alpha}^{(n)}, \widehat{h}^{(n)}_\tau), \boldsymbol{F}_2(\boldsymbol{\alpha}^{(n)}, \widehat{h}^{(n)}_\tau)\right) = \boldsymbol{0}$
    Compute $\boldsymbol{\alpha}^{(n+1)}$ as

$$\boldsymbol{\alpha}^{(n+1)} = \boldsymbol{\alpha}^{(n)} - \nabla_{\boldsymbol{\alpha}} \boldsymbol{F}_3(\boldsymbol{\alpha}^{(n)}, \widehat{h}^{(n)}_\tau)^{-1} \boldsymbol{F}_3(\boldsymbol{\alpha}^{(n)}, \widehat{h}^{(n)}_\tau)$$

  until $\|\nabla_{\boldsymbol{\alpha}} \boldsymbol{F}_3(\boldsymbol{\alpha}^{(n+1)}, \widehat{h}^{(n+1)}_\tau)^{-1} \boldsymbol{F}_3(\boldsymbol{\alpha}^{(n+1)}, \widehat{h}^{(n+1)}_\tau)\|_\infty \leq \tau_g^{p+1}$
  Refine $\mathcal{S}^p_{\tau_g}$ and $\mathcal{S}^p_{\tau_h}$
until $\tau_g \leq \tau_{\min}$

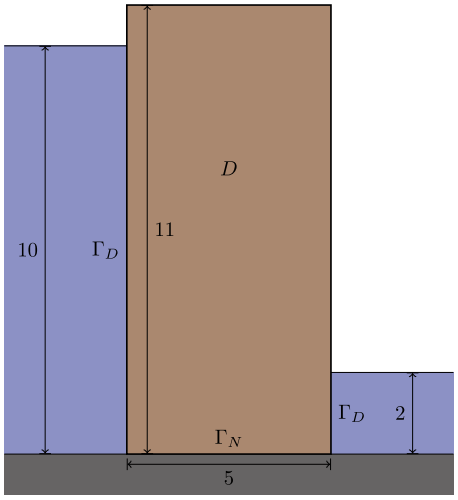

Fig. 5. Homogeneous rectangular dam.

Table 1
Number of required iterations and errors on the boundary conditions for the homogeneous rectangular dam.

	$\tau_g = 2^{-1}$	$\tau_g = 2^{-2}$	$\tau_g = 2^{-3}$	$\tau_g = 2^{-4}$	$\tau_g = 2^{-5}$	$\tau_g = 2^{-6}$
N_{iter}	3	5	2	3	8	8
$\|K\nabla h \cdot \boldsymbol{n}\|_{L^2(\Gamma_F)}$	2.34	$6.00 \cdot 10^{-2}$	$2.80 \cdot 10^{-2}$	$2.55 \cdot 10^{-2}$	$3.99 \cdot 10^{-3}$	$1.11 \cdot 10^{-3}$
$\|h - x_d\|_{L^\infty(\Gamma_F)}$	1.31	$1.26 \cdot 10^{-1}$	$6.54 \cdot 10^{-2}$	$2.33 \cdot 10^{-2}$	$6.64 \cdot 10^{-3}$	$1.71 \cdot 10^{-3}$

5. Numerical results

In this section, we present a comprehensive analysis that demonstrates the accuracy and reliability of our proposed method in effectively handling various unconfined water flow problems, including both two-dimensional and three-dimensional cases. At this stage of investigation we disregard those aspects related to slope stability. To simplify our tests, we consider no recharge by setting $\boldsymbol{r} = \boldsymbol{0}$, we set the base of the dam as the impervious boundary Γ_N and we only consider isotropic hydraulic conductivity $\boldsymbol{K} = K\mathbb{I}$, where $K \in L^\infty(D, \mathbb{R})$ and $\mathbb{I} \in \mathbb{R}^{d\times d}$ denotes the identity matrix.

Throughout our experiments, we employ C^1-continuous quadratic splines and report the errors in the L^2-norm and L^∞-norm, respectively, for the Neumann and Dirichlet boundary conditions on Γ_F at the final iteration of each refinement step.

For bi-dimensional problems, we provide visualizations of the piezometric head and the flux in the wet region, obtained at the final iteration of each refinement step. On the other hand, for the three-dimensional examples, we present the phreatic surface achieved at the final iteration of each refinement step. Furthermore, for the finest solution, we showcase the piezometric head and the flux in selected bi-dimensional sections of the wet region.

5.1. 2D homogeneous rectangular dam

As a first example, we examine the same two-dimensional rectangular dam considered in [15], see Fig. 5. To replicate the exact solution reported in [15], we utilize a homogeneous hydraulic conductivity parameter $K = 1$ and apply water level conditions of $\ell = 10$ on the left vertical side and $\ell = 2$ on the right vertical side. The convergence of the wet region can be observed in Fig. 6 where it becomes evident that the wet region reaches stability rapidly as we refine the spline spaces. Additionally, Table 1 showcases the reduction in errors for both the Neumann and Dirichlet boundary conditions as we reduce the mesh size. This analysis demonstrates that our model's behavior aligns with the findings of [15] and validates the accuracy of our approach in solving the problem at hand. Finally, in Fig. 7 we report the convergence history of the L^∞-norm of the residual $\boldsymbol{F}_3(\boldsymbol{\alpha}^{(n)}, \widehat{h}^{(n)}_\tau)$.

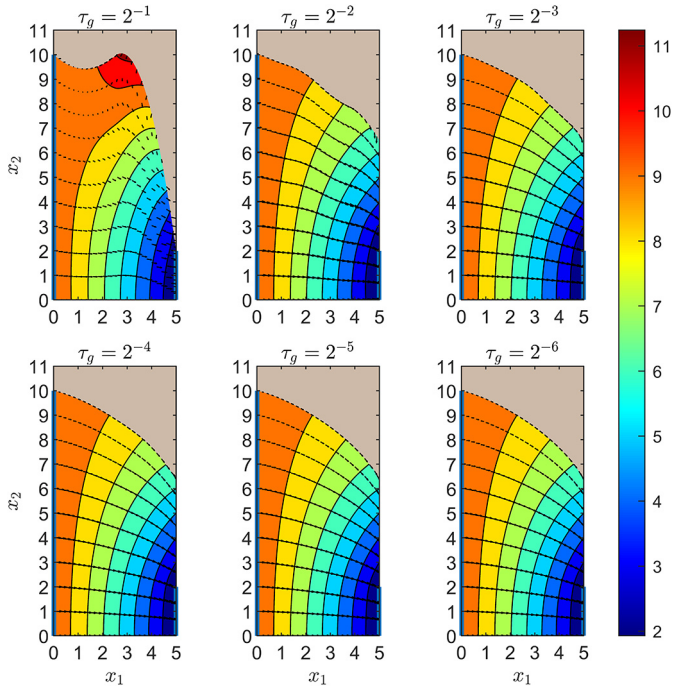

Fig. 6. Piezometric head and flux for the homogeneous rectangular dam at the final iteration for each mesh-size τ_g.

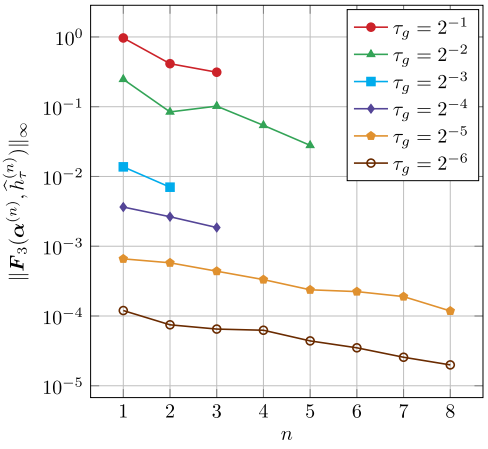

Fig. 7. L^∞-norm of the residual plotted against the iterations for the homogeneous rectangular dam.

Table 2
Number of required iterations and errors on the boundary conditions for the homogeneous trapezoidal dam.

	$\tau_g = 2^{-1}$	$\tau_g = 2^{-2}$	$\tau_g = 2^{-3}$	$\tau_g = 2^{-4}$	$\tau_g = 2^{-5}$	$\tau_g = 2^{-6}$
N_{iter}	2	4	5	8	9	9
$\|K\nabla h \cdot \boldsymbol{n}\|_{L^2(\Gamma_F)}$	$6.25 \cdot 10^{-1}$	$5.24 \cdot 10^{-2}$	$4.26 \cdot 10^{-3}$	$2.40 \cdot 10^{-4}$	$5.80 \cdot 10^{-4}$	$6.35 \cdot 10^{-4}$
$\|h - x_d\|_{L^\infty(\Gamma_F)}$	$3.89 \cdot 10^{-1}$	$1.72 \cdot 10^{-1}$	$5.65 \cdot 10^{-2}$	$1.36 \cdot 10^{-2}$	$3.58 \cdot 10^{-3}$	$8.29 \cdot 10^{-4}$

5.2. 2D homogeneous trapezoidal dam

The second example focuses on the same two-dimensional trapezoidal dam examined in [15], see Fig. 8. Also in this case, to reproduce the exact solution reported in [15], we use a homogeneous hydraulic conductivity parameter of $K = 1$ and impose water level conditions of $\ell = 5$ on the left vertical side and $\ell = 1$ on the right vertical side. Similarly to the previous example, the wet region rapidly converges to a solution comparable to the one obtained in [15], see Fig. 9. Moreover, in Table 2 we observe that the finest solution achieves very small errors. Finally, in Fig. 10 we report the convergence history of the L^∞-norm of the residual $\boldsymbol{F}_3(\boldsymbol{\alpha}^{(n)}, \widehat{h}_\tau^{(n)})$.

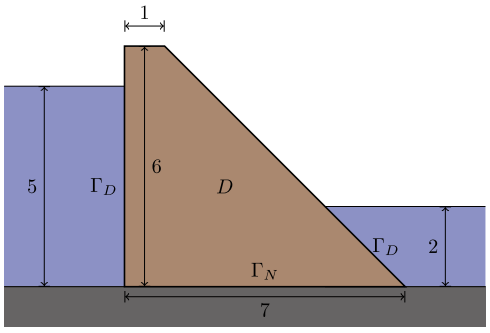

Fig. 8. Homogeneous trapezoidal dam.

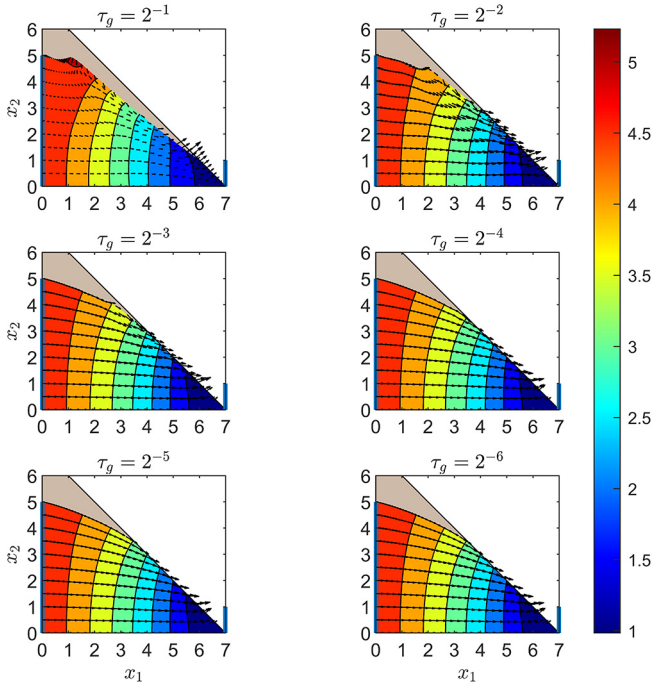

Fig. 9. Piezometric head and flux for the trapezoidal dam at the final iteration for each mesh-size τ_g.

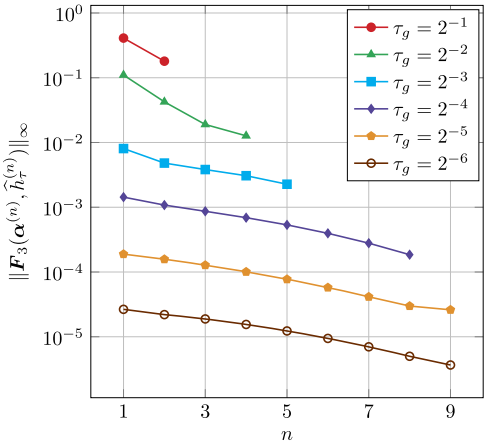

Fig. 10. L^∞-norm of the residual plotted against the iterations for the homogeneous trapezoidal dam.

5.3. 2D non homogeneous rectangular dam

The last two-dimensional example addresses the same problem of non-homogeneous hydraulic conductivity as considered in [4], see Fig. 11. Specifically, we set

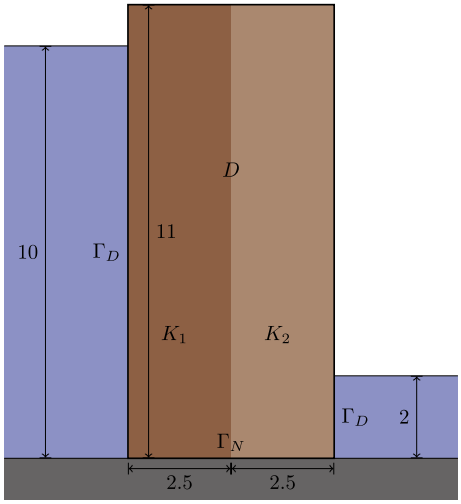

Fig. 11. Non-homogeneous rectangular dam.

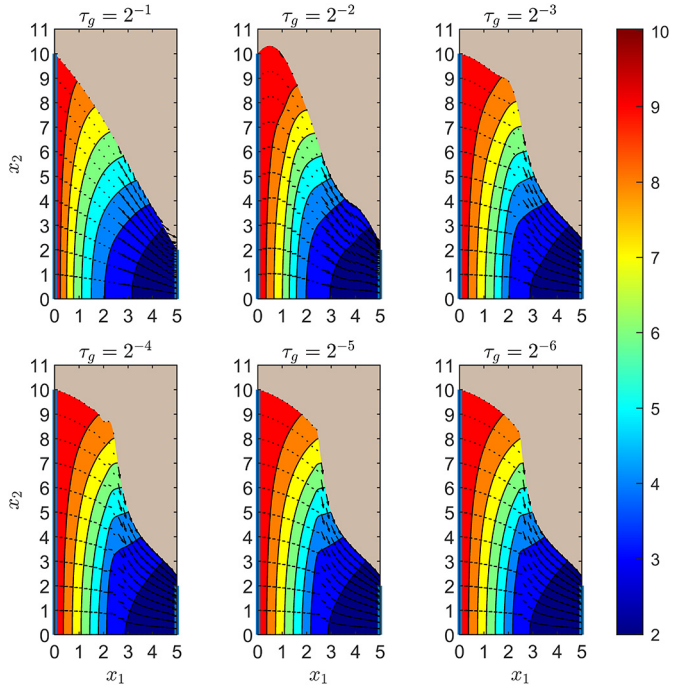

Fig. 12. Piezometric head and flux for the non-homogeneous rectangular dam at the final iteration for each mesh-size τ_g.

Table 3
Number of required iterations and errors on the boundary conditions for the non-homogeneous rectangular dam.

	$\tau_g = 2^{-1}$	$\tau_g = 2^{-2}$	$\tau_g = 2^{-3}$	$\tau_g = 2^{-4}$	$\tau_g = 2^{-5}$	$\tau_g = 2^{-6}$
N_{iter}	1	2	6	8	16	22
$\|K\nabla h \cdot \boldsymbol{n}\|_{L^2(\Gamma_F)}$	$3.41 \cdot 10^{1}$	2.89	1.45	$3.85 \cdot 10^{-1}$	$1.64 \cdot 10^{-1}$	$5.27 \cdot 10^{-2}$
$\|h - x_d\|_{L^\infty(\Gamma_F)}$	$1.85 \cdot 10^{-1}$	$3.38 \cdot 10^{-1}$	$6.08 \cdot 10^{-2}$	$1.70 \cdot 10^{-2}$	$4.40 \cdot 10^{-3}$	$1.66 \cdot 10^{-3}$

$$K(x_1, x_2) = \begin{cases} K_1 = 1, & \text{for } x_1 \in [0, \frac{5}{2}), \\ K_2 = 10, & \text{for } x_1 \in [\frac{5}{2}, 5], \end{cases}$$

and impose water level conditions of $\ell = 10$ on the left vertical side and $\ell = 2$ on the right vertical side. Although this example required slightly more iterations than the one presented in Section 5.1, Fig. 12 illustrates that our method produces a solution almost identical to the one shown in [4]. This is further supported by the low errors reported in Table 3. Finally, in Fig. 13 we report the convergence history of the L^∞-norm of the residual $\boldsymbol{F}_3(\boldsymbol{\alpha}^{(n)}, \widehat{h}_\tau^{(n)})$.

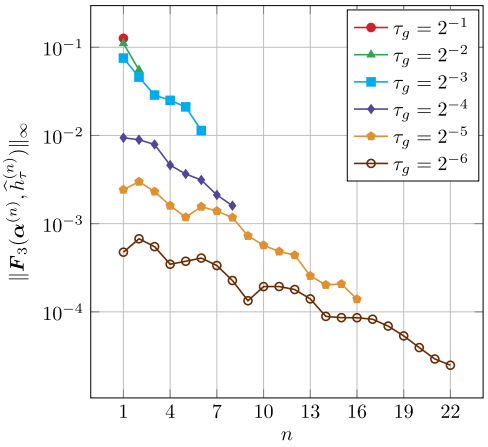

Fig. 13. L^∞-norm of the residual plotted against the iterations for the non-homogeneous rectangular dam.

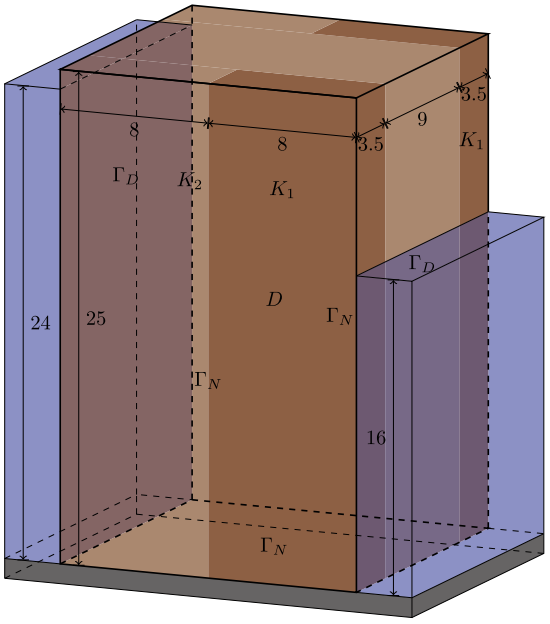

Fig. 14. Non-homogeneous rectangular cuboid shaped dam.

5.4. 3D dam with discontinuous hydraulic conductivity

As an example of a three-dimensional problem, we consider a rectangular cuboid, as shown in Fig. 14, with non-homogeneous hydraulic conductivity. Specifically, to align with the same framework used in [4], we set

$$K(x_1, x_2, x_3) = \begin{cases} K_1 = 1, & \text{for } x_1 \in [0, \frac{7}{2}] \cup [\frac{25}{2}, 16],\ x_2 \in [8, 16], \\ K_2 = 10, & \text{otherwise.} \end{cases}$$

The imposed water levels are $\ell = 24$ on the vertical side $\boldsymbol{x} = (x_1, x_2, x_3) \in \mathbb{R}^3 :\ x_1 = 0$ and $\ell = 16$ on the opposite side $\boldsymbol{x} = (x_1, x_2, x_3) \in \mathbb{R}^3 :\ x_1 = 16$. The phreatic surface depicted in Fig. 15 bears a striking resemblance to the one presented in [4]. Additionally, Table 4 exhibits errors that steadily decrease as we refine the spline spaces. The favorable behavior of our method is also evident in Figs. 17 and 18, where we have depicted the piezometric head and the flux for several sections of the wet region. Finally, in Fig. 16 we report the convergence history of the L^∞-norm of the residual $\boldsymbol{F}_3(\boldsymbol{\alpha}^{(n)}, \widehat{h}_\tau^{(n)})$.

5.5. 3D homogeneous NURBS parametrized dam

Finally, let us consider the last example, which involves a NURBS-parametrized three-dimensional dam with homogeneous hydraulic conductivity, as illustrated in Fig. 19. For this scenario, we impose specific water level conditions of $\ell = 1.9$ on the external arched lateral side and $\ell = 0.5$ on the internal one. Although we lack a reference solution for comparison, the remarkably small errors reported in Table 5, along with the well-defined

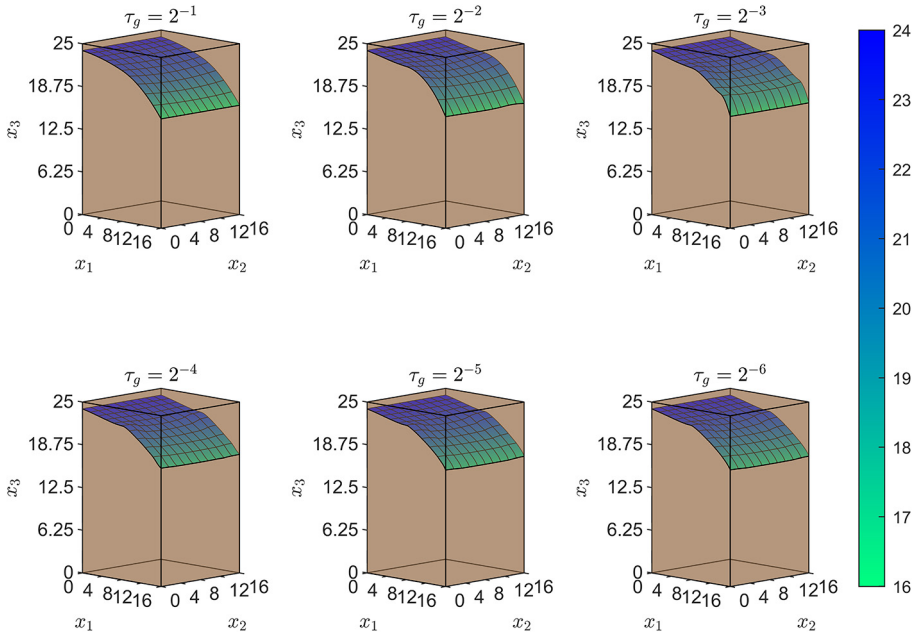

Fig. 15. Phreatic surface for the rectangular cuboid shaped dam at the final iteration for each mesh-size τ_g.

Table 4
Number of required iterations and errors on the boundary conditions for the non-homogeneous rectangular cuboid shaped dam.

	$\tau_g = 2^{-1}$	$\tau_g = 2^{-2}$	$\tau_g = 2^{-3}$	$\tau_g = 2^{-4}$	$\tau_g = 2^{-5}$	$\tau_g = 2^{-6}$
N_{iter}	1	1	2	8	8	8
$\|K\nabla h \cdot \boldsymbol{n}\|_{L^2(\Gamma_F)}$	$1.33 \cdot 10^{2}$	$8.06 \cdot 10^{1}$	$7.95 \cdot 10^{1}$	$1.06 \cdot 10^{1}$	$1.24 \cdot 10^{-1}$	$9.32 \cdot 10^{-2}$
$\|h - x_d\|_{L^\infty(\Gamma_F)}$	$4.52 \cdot 10^{-1}$	$4.07 \cdot 10^{-1}$	$3.61 \cdot 10^{-1}$	$7.77 \cdot 10^{-2}$	$2.81 \cdot 10^{-2}$	$2.66 \cdot 10^{-3}$

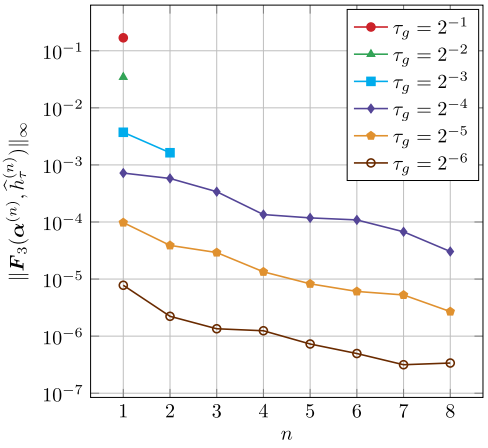

Fig. 16. L^∞-norm of the residual plotted against the iterations for the non-homogeneous rectangular cuboid shaped dam.

phreatic surface shown in Fig. 20, and the piezometric head and flux depicted in Fig. 22, all provide compelling evidence that our method yields a physically consistent solution. Finally, in Fig. 21 we report the convergence history of the L^∞-norm of the residual $\boldsymbol{F}_3(\boldsymbol{\alpha}^{(n)}, \widehat{h}_\tau^{(n)})$.

6. Conclusions

In this work we have introduced a shape optimization based isogeometric method for the determination of the steady groundwater flow in saturated porous media. The applicability and effectiveness of the proposed method are demonstrated through several benchmark problems, including highly non-homogeneous hydraulic conductivity. For both the 2D and 3D cases, our quasi-Newton iterations produce solution comparable to those in the literature. Finally, for what concern the computational cost, we underline that the algorithm proposed can be performed efficiently exploiting suitable linear solvers specifically designed for isogeometric analysis.

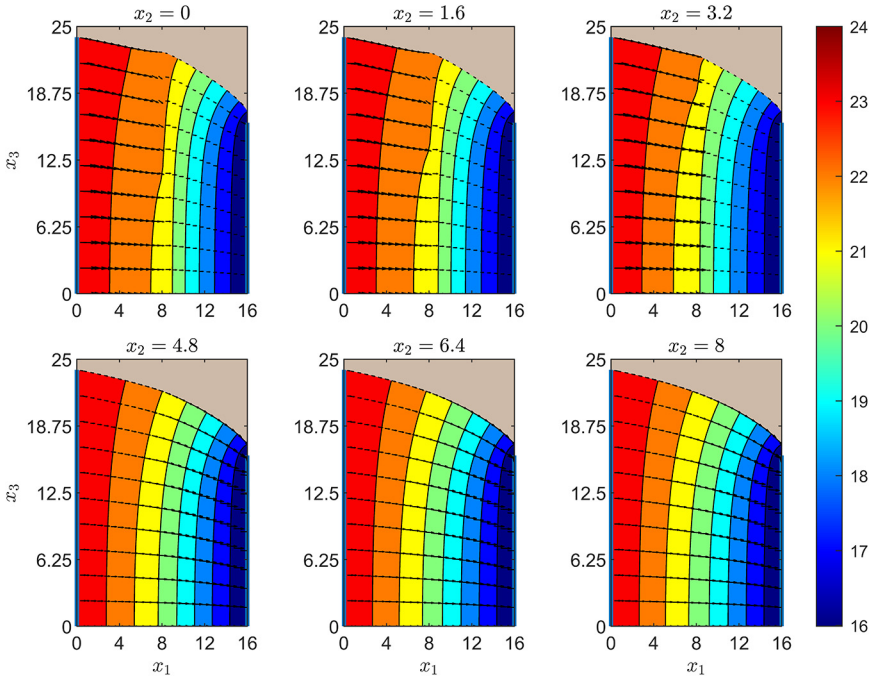

Fig. 17. Piezometric head and flux for the rectangular cuboid shaped dam at different domain sections for the final iteration on the finest discretization.

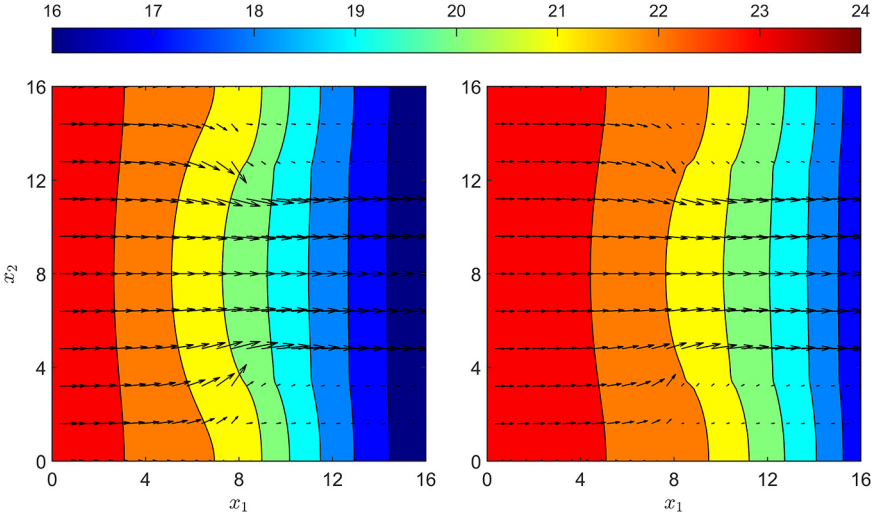

Fig. 18. Piezometric head and flux at the base of the dam (left) and on the phreatic surface (right) for the rectangular cuboid shaped dam for the final iteration on the finest discretization.

Table 5
Number of required iterations and errors on the boundary conditions for the homogeneous NURBS parametrized dam.

	$\tau_g = 2^{-1}$	$\tau_g = 2^{-2}$	$\tau_g = 2^{-3}$	$\tau_g = 2^{-4}$	$\tau_g = 2^{-5}$	$\tau_g = 2^{-6}$
N_{iter}	2	4	3	9	11	15
$\|K\nabla h \cdot \boldsymbol{n}\|_{L^2(\Gamma_F)}$	1.20	$5.99 \cdot 10^{-2}$	$1.43 \cdot 10^{-2}$	$1.23 \cdot 10^{-3}$	$2.87 \cdot 10^{-4}$	$7.69 \cdot 10^{-5}$
$\|h - x_d\|_{L^\infty(\Gamma_F)}$	$2.53 \cdot 10^{-1}$	$1.25 \cdot 10^{-1}$	$3.21 \cdot 10^{-2}$	$7.59 \cdot 10^{-3}$	$2.02 \cdot 10^{-3}$	$6.45 \cdot 10^{-4}$

Data availability

No data was used for the research described in the article.

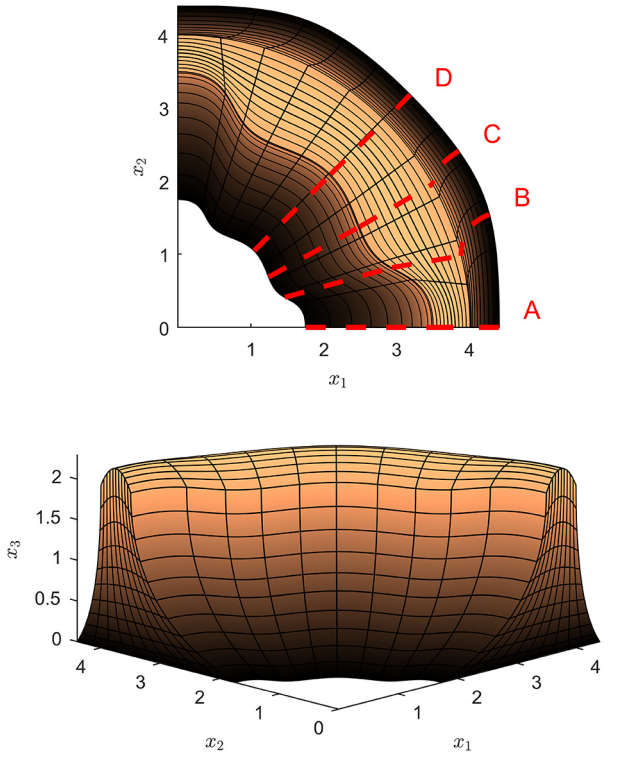

Fig. 19. Homogeneous NURBS parametrized dam.

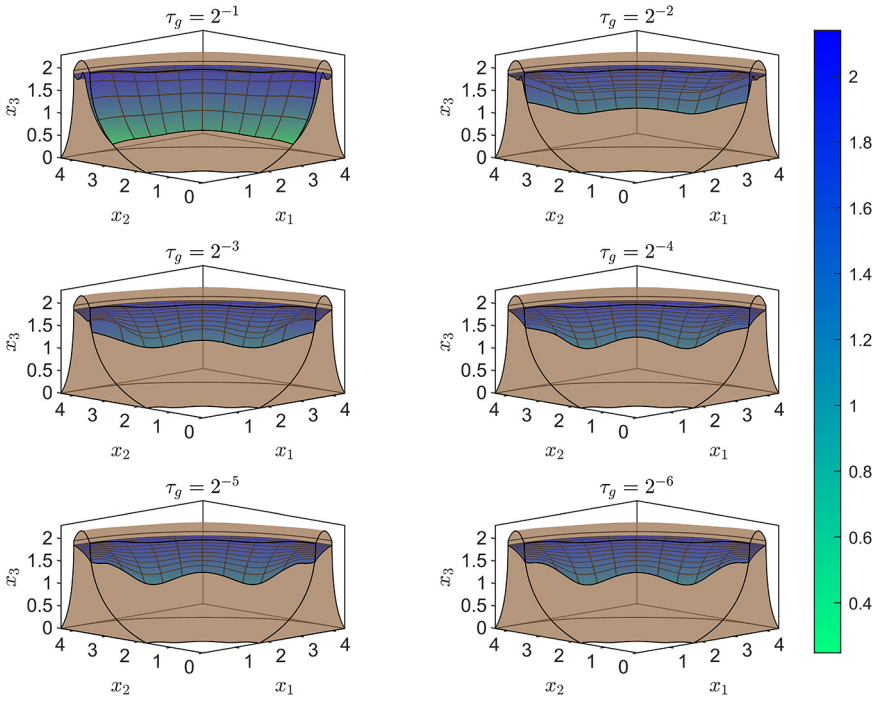

Fig. 20. Phreatic surface for the NURBS dam at the final iteration for each mesh-size τ_g.

Acknowledgements

Support for this research was partially provided by a grant through Regione Lombardia, POR FESR 2014-2020 - Call HUB Ricerca e Innovazione, Progetto 1139857 CE4WE: Approvvigionamento energetico e gestione della risorsa idrica nell'ottica dell'Economia Circolare (Circular Economy for Water and Energy). A. Bressan and A. Reali acknowledge the contribution of the Italian Ministry of University and Research (MUR) through the PRIN project COSMIC (No. 2022A79M75), funded by the European Union - Next Generation EU. S. Manenti and A. Bressan acknowledge the support of the project PRIN PNRR "Uncertainty Quantification of coupled models for water flow and contaminant transport" (P2022LXLYY), financed by the European Union - NextGeneration EU. G. Loli, S. Manenti, A. Reali and G. Sangalli also acknowledge support from PNRR-M4C2-

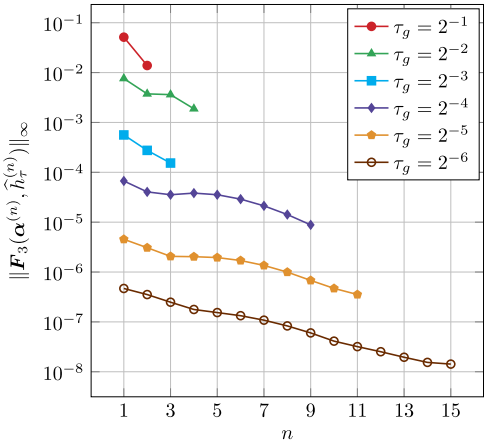

Fig. 21. L^∞-norm of the residual plotted against the iterations for the homogeneous NURBS parametrized dam.

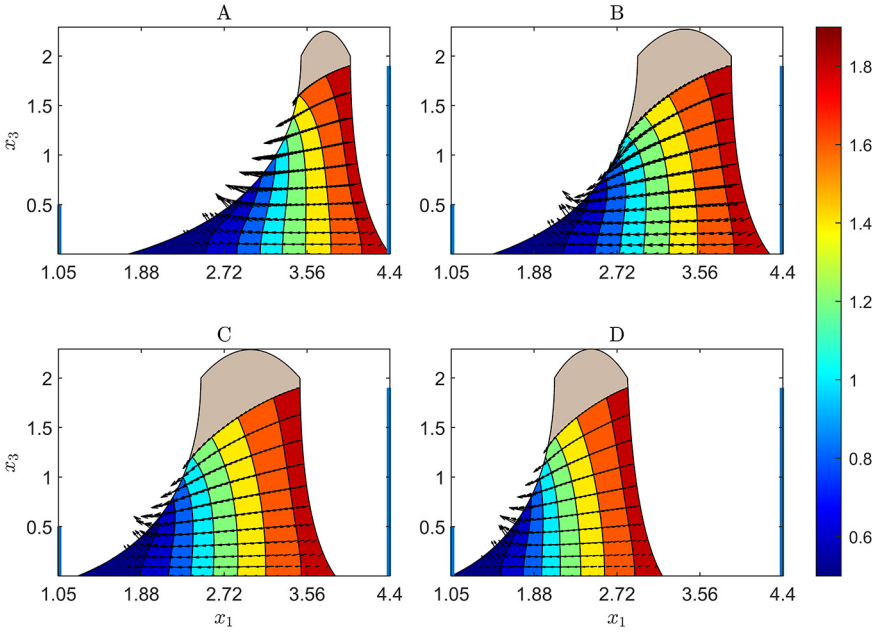

Fig. 22. Piezometric head and flux for the NURBS dam at different sections of the wet region (depicted with red dashed lines in Fig. 19) for the final iteration on the finest discretization.

I1.4-NC-HPC-Spoke6. A. Bressan is also funded by the European Union - NextGenerationEU and by the Ministry of University and Research (MUR), National Recovery and Resilience Plan (NRRP), Mission 4, Component 2, Investment 1.5, project "RAISE - Robotics and AI for Socio-economic Empowerment" (ECS00000035). A. Reali and G. Sangalli acknowledge the support of the Italian Ministry of University and Research (MUR) through the PRIN 2022 PNRR project NOTES (No. P2022NC97R), funded by the European Union - Next Generation EU. A. Bressan, G. Loli, A. Reali and G. Sangalli are members of the Gruppo Nazionale Calcolo Scientifico-Istituto Nazionale di Alta Matematica (GNCS-INDAM).

References

[1] H.W. Alt, Numerical solution of steady-state porous flow free boundary problems, Numer. Math. 36 (1980) 73–98.
[2] J. Bear, Dynamics of Fluids in Porous Media, Courier Corporation, 1988.
[3] Jacob Bear, Yehuda Bachmat, Introduction to Modeling of Transport Phenomena in Porous Media, vol. 4, Springer Science & Business Media, 2012.
[4] E. Bresciani, P. Davy, J.R. de Dreuzy, A finite volume approach with local adaptation scheme for the simulation of free surface flow in porous media, Int. J. Numer. Anal. Methods Geomech. 36 (13) (2012) 1574–1591.
[5] A. Bressan, E. Sande, Approximation in FEM, DG and IGA: a theoretical comparison, Numer. Math. (2019).
[6] J.A. Cottrell, T.J.R. Hughes, Y. Bazilevs, Isogeometric Analysis: Toward Integration of CAD and FEA, John Wiley & Sons, Chichester, 2009.
[7] C. De Boor, A Practical Guide to Splines, revised edition, Applied Mathematical Sciences, vol. 27, Springer-Verlag, New York, 2001.
[8] M.C. Delfour, J.-P. Zolésio, Shapes and Geometries: Metrics, Analysis, Differential Calculus, and Optimization, SIAM, 2011.

[9] K. Eppler, H. Harbrecht, Shape optimization for free boundary problems–analysis and numerics, in: Constrained Optimization and Optimal Control for Partial Differential Equations, 2012, pp. 277–288.
[10] J.A. Evans, Y. Bazilevs, I. Babuška, T.J.R. Hughes, n-widths, sup-infs, and optimality ratios for the k-version of the isogeometric finite element method, Comput. Methods Appl. Mech. Eng. 198 (2009) 1726–1741.
[11] R. Glowinski, J.-P. Zolesio, Free and Moving Boundaries: Analysis, Simulation and Control, CRC Press, 2007.
[12] M.E. Harr, Groundwater and Seepage, Courier Corporation, 1991.
[13] T.J.R. Hughes, J.A. Cottrell, Y. Bazilevs, Isogeometric analysis: CAD, finite elements, NURBS, exact geometry and mesh refinement, Comput. Methods Appl. Mech. Eng. 194 (39) (2005) 4135–4195.
[14] K.T. Kärkkäinen, T. Tiihonen, Free surfaces: shape sensitivity analysis and numerical methods, Int. J. Numer. Methods Eng. 44 (8) (1999) 1079–1098.
[15] M.J. Kazemzadeh-Parsi, Isogeometric analysis in solution of unconfined seepage problems, Comput. Math. Appl. (ISSN 0898-1221) 78 (1) (2019) 66–80.
[16] G. Loli, G. Sangalli, M. Tani, Easy and efficient preconditioning of the isogeometric mass matrix, in: New Trends in Computational Methods for PDEs, Comput. Math. Appl. (ISSN 0898-1221) 116 (2022) 245–264.
[17] L.D. Marini, P. Pietra, Fixed-point algorithms for stationary flow in porous media, Comput. Methods Appl. Mech. Eng. (ISSN 0045-7825) 56 (1) (1986) 17–45.
[18] M. Montardini, F. Remonato, G. Sangalli, Isogeometric methods for free boundary problems, in: Harald van Brummelen, Cornelis Vuik, Matthias Möller, Clemens Verhoosel, Bernd Simeon, Bert Jüttler (Eds.), Isogeometric Analysis and Applications 2018, Springer International Publishing, Cham, ISBN 978-3-030-49836-8, 2021, pp. 131–155.
[19] M.N. Nguyen, T.Q. Bui, T. Yu, S. Hirose, Isogeometric analysis for unsaturated flow problems, Comput. Geotech. 62 (2014) 257–267.
[20] L. Piegl, W. Tiller, The NURBS Book, Springer, 1997.
[21] Karsten Pruess, Curtis M. Oldenburg, G.J. Moridis, TOUGH2 user's guide version 2, Tech. Rep., Lawrence Berkeley National Lab. (LBNL), Berkeley, CA (United States), 1999.
[22] Nicolò Salis, Alessandro Franci, Sergio Idelsohn, Alessandro Reali, Sauro Manenti, Lagrangian particle-based simulation of waves: a comparison of SPH and PFEM approaches, Eng. Comput. (2023) 1–15.
[23] Nicolò Salis, Xiangyu Hu, Min Luo, Alessandro Reali, Sauro Manenti, 3D SPH analysis of focused waves interacting with a floating structure, Appl. Ocean Res. (ISSN 0141-1187) 144 (2024) 103885, https://doi.org/10.1016/j.apor.2024.103885, https://www.sciencedirect.com/science/article/pii/S0141118724000075.
[24] Nicolò Salis, Min Luo, Alessandro Reali, Sauro Manenti, Wave generation and wave–structure impact modelling with WCSPH, Ocean Eng. (ISSN 0029-8018) 266 (2022) 113228, https://doi.org/10.1016/j.oceaneng.2022.113228, https://www.sciencedirect.com/science/article/pii/S0029801822025112.
[25] G. Sangalli, M. Tani, Isogeometric preconditioners based on fast solvers for the Sylvester equation, SIAM J. Sci. Comput. 38 (6) (2016) A3644–A3671.
[26] S. Shahrokhabadi, T.D. Cao, F. Vahedifard, Thermo-hydro-mechanical modeling of unsaturated soils using isogeometric analysis: model development and application to strain localization simulation, Int. J. Numer. Anal. Methods Geomech. 44 (2) (2020) 261–292.
[27] S. Shahrokhabadi, F. Vahedifard, M. Bhatia, Head-based isogeometric analysis of transient flow in unsaturated soils, Comput. Geotech. (ISSN 0266-352X) 84 (2017) 183–197.
[28] J. Sokolowski, J.-P. Zolésio, Introduction to Shape Optimization, Springer, 1992.
[29] J.-M. Vanden-Broeck, Gravity-Capillary Free-Surface Flows, Cambridge University Press, 2010.
[30] K.G. Van der Zee, E.H. Van Brummelen, R. de Borst, Goal-oriented error estimation and adaptivity for free-boundary problems: the shape-linearization approach, SIAM J. Sci. Comput. 32 (2) (2010) 1093–1118.
[31] K.G. Van der Zee, G.J. Van Zwieten, C.V. Verhoosel, E.H. Van Brummelen, Shape-Newton method for isogeometric discretizations of free-boundary problems, in: MARINE 2011, IV International Conference on Computational Methods in Marine Engineering: Selected Papers, Springer, 2013, pp. 85–102.